Remote Sensing of Environment 251 (2020) 112057

Contents lists available at ScienceDirect

Remote Sensing of Environment

journal homepage: www.elsevier.com/locate/rse

Internal kinematics of the Slumgullion landslide (USA) from high-resolution UAVSAR InSAR data

Xie Hu[a,b,*,1], Roland Bürgmann[a,b], Eric J. Fielding[c], Hyongki Lee[d]

[a] Berkeley Seismological Laboratory, University of California, Berkeley, CA, USA
[b] Department of Earth and Planetary Science, University of California, Berkeley, CA, USA
[c] Jet Propulsion Laboratory, California Institute of Technology, Pasadena, CA, USA
[d] Department of Civil and Environmental Engineering, University of Houston, Houston, TX, USA

ARTICLE INFO

Keywords:
Slumgullion landslide
Kinematic boundaries
Geomorphologic features
UAVSAR
InSAR

ABSTRACT

Landslides represent one of the most damaging natural hazards and often lead to unexpected casualties and property damage. They also continually modify our natural environment and landscapes. Knowledge of landslide systems is largely restricted by the stochastic nature, subjective interpretation and infrequent or spatially sparse surveying of landslides. Characterized by persistent daily movements of a couple of centimeters over multi-centennial timescales and a long narrow shape as long as ~4 km, the Slumgullion landslide in Colorado, USA represents an ideal natural laboratory to study slow-moving landslides. Here we demonstrate the capability of the highly accurate, spatially continuous airborne Synthetic Aperture Radar (SAR) system of the NASA Uninhabited Aerial Vehicle SAR (UAVSAR) to characterize the kinematic details of internal deformation of the Slumgullion landslide using SAR interferometry (InSAR). We develop a phase-based approach to automatically extract the boundaries of the mobile geological structures without unwrapping. Comparison with historic field observations from 1991 reveals the 40-m advance of the frontal toe and shift of an internal fault. The UAVSAR data also resolve an internal minislide (100 by 70 m), which moves more southerly than the main body at 5 mm/day in the lower part of the landslide. A Light Detection and Ranging (LiDAR) Digital Elevation Model (DEM) shows that the minislide is associated with the opening of a 30 by 10 m pull-apart basin and bounding strike-slip faults. These extensional structures, nearby incised streams, and steepened local slopes helped establish the kinematic environment for the formation of the secondary minislide. The disparity between the UAVSAR InSAR-derived horizontal moving directions and the LiDAR DEM-derived slope aspects suggest that while the surface topography governs the first-order orientation, the local kinematics is also subject to the variable nature of heterogeneous landslide materials and the irregular basal bedrock surface. The landslide velocity and precipitation show similar multi-annual variations. Our study demonstrates that the freely available, high-resolution UAVSAR data, have great potential for characterizing landslide kinematics and other small-scale geological and geomorphological processes.

1. Introduction

Landslides represent important mass wasting processes that reshape global landscapes by efficiently delivering earth materials to river channels and continued downstream transport. Landslides also present natural hazards — catastrophic failures may threaten people's lives and damage properties. Like all the Earth's surface processes, various environmental and geological factors regulate landslide properties and behaviors (e.g., Handwerger et al., 2019a; Hu et al., 2019; Shi et al., 2019; Wang et al., 2018c). Landslides can be categorized into two groups in terms of their mobility. Dynamic failures may lead to sudden destruction and casualties, by the slope failure itself or from subsequent secondary hazards such as stream blockages, flooding and inundation. On the other hand, slow-moving landslides can produce substantial damage, but rarely result in lethal consequences; however, they have the potential to transform into dynamic acceleration or failures due to extreme weather events or strong earth shaking (e.g., Lacroix et al., 2020; Lacroix et al., 2015; Handwerger et al., 2019a; Kang et al., 2019). Slow-moving landslides are usually hydrologically controlled (e.g., Iverson et al., 2000; Hu et al., 2018a). Water and thus the pore pressure

* Corresponding author at: Berkeley Seismological Laboratory, University of California, Berkeley, CA, USA.
E-mail address: xiehu@uh.edu (X. Hu).
[1] Current address: Department of Civil and Environmental Engineering, University of Houston, Houston, TX, USA.

https://doi.org/10.1016/j.rse.2020.112057
Received 16 April 2020; Received in revised form 4 August 2020; Accepted 23 August 2020
Available online 29 August 2020
0034-4257/ © 2020 Elsevier Inc. All rights reserved.

beneath the surface is the essential agent to alter the resistance to the gravitational driving force and mobilize the system. In landslide-prone terrain with cyclic water recharge, the downslope movements often also reveal periodic variations which may lag behind the meteorological record due to the progressive generation and dissipation of pore pressures from the ground surface to the basal beds (e.g., Handwerger et al., 2016; Cohen-Waeber et al., 2018; Hu et al., 2019). Besides the well-established linkage between water recharge and landslide speed, slide-internal structures, such as tensile fissures and faults, may also modulate this behavior (Handwerger et al., 2019b; Krzeminska et al., 2013).

Remote sensing data of optical imagery, Light Detection and Ranging (LiDAR), and Synthetic Aperture Radar (SAR) have been widely used for landslide mapping. Optical imagery has been mainly used to identify the failures and assess the secondary hazards; however, optical imagery is ineffective under inclement weather conditions; in addition, it cannot unveil the geomorphological details for vegetated slopes. LiDAR sensors deployed on the ground or from unmanned aerial vehicles are labor intensive and permit a limited distance of illuminating areas. Even for LiDAR mapping from a low altitude aircraft in ideal weather, which is usually for the landslide study, the swath width is only a few hundred of meters. Thus, costly LiDAR surveys are not practical to monitor the landslide evolution in a frequent manner. Interferometric SAR (InSAR) measures the regional ground displacement from the phase difference between SAR images collected at different times, and it has been used in numerous geohazard applications including landslides, taking advantage of the all-weather, day-and-night, and regular acquisition routine (e.g., Bürgmann et al., 2000; Dong et al., 2018; Hu et al., 2017; Kim et al., 2015; Lu and Dzurisin, 2014; Wang et al., 2018b). Pixel cross-correlation analysis can be applied to both optical images and SAR amplitude images. The accuracy and feasibility are determined by the spatial resolution of the remote sensing data and the displacement gradient of the area of interest. High-resolution optical images such as Sentinel-2, Landsat 7/8 and Planet allows for abrupt change detection in velocity of ~1 m/day (Lacroix et al., 2020); airborne UAVSAR data allows for capturing moderate motions of a few cm/day (Hu et al., 2020).

The Slumgullion landslide is a translational earth slide in the San Juan Mountains in Hinsdale County, southwestern Colorado, USA (e.g., Crandell and Varnes, 1961; Endlich, 1876; Fleming et al., 1996; Fleming et al., 1999; Gomberg et al., 1995; Parise and Guzzi, 1992). The area of landslide deposits is composed of two distinct parts (Fig. 1). The first part, stretching from the headscarp on the edge of the Cannibal Plateau to the Lake Fork of the Gunnison River, is about 700 years old, as determined by radiocarbon dating of wood and soil humus at the toe, and is currently inactive. Lake San Cristobal was formed by damming of the river by the old landslide mass. The second part has reactivated entirely within the upper portion of the old landslide deposits along a distance of ~4 km from the original headscarp to a new toe 200 m above State Highway 149 for the past 300 years as dated by tree rings. A prehistoric Slumgullion landslide failure dammed Lake San Cristobal that is 1.5 km further downhill with some lodges built on the lakeshore. The persistent movements of this system at a couple of centimeters per day for the fastest middle segment make the Slumgullion an ideal natural laboratory for studying slow-moving landslides (e.g., Fleming et al., 1999). It is also one of the best-studied and well-instrumented landslides in the world.

Previous studies at the Slumgullion landslide focused on quantifying the magnitude of the movements. The interactions between kinematic structures within the landslide have not been well explored due to insufficient resolution. To better understand the kinematic expressions of the Slumgullion, we exploit all the archived NASA Uninhabited Aerial Vehicle SAR (UAVSAR) data acquired during 2011–2018. We propose a simple and straightforward method to extract the kinematic elements (KEs) from the interferograms without phase unwrapping, validated by previously defined KEs based solely on the distribution of mapped internal fault structures. We also derive the complete three-dimensional (3D) surface displacements during 16 independent, short time periods (3–16 days), and reveal an apparent first-order correlation between the average daily rate and the inferred water recharge and pore pressure. Integrated with the morphologic features of a pull-apart basin revealed by a LiDAR bare-earth Digital Elevation Model (DEM), we explore the conditions allowing for the formation of a secondary "minislide" near the margin of the main body of the Slumgullion. Finally, we compare the horizontal vectors from InSAR-derived complete 3D displacements with the DEM-derived slope aspects.

2. Background of the Slumgullion landslide

2.1. Geological setting

The good exposure of the Slumgullion landslide allows us to identify a fairly complete collection of geological and kinematic features that are familiar from crustal-scale tectonics and can be recognized within this natural laboratory, including scarps, lobes, hummocks, depressions, flank ridges, benches, risers, tensile cracks and extensional normal faults, as well as contractional thrust structures traversing the landslide. Strike-slip structures accommodate shear along the lateral margins and within the slide mass (e.g., Gomberg et al., 1995). The kinematic

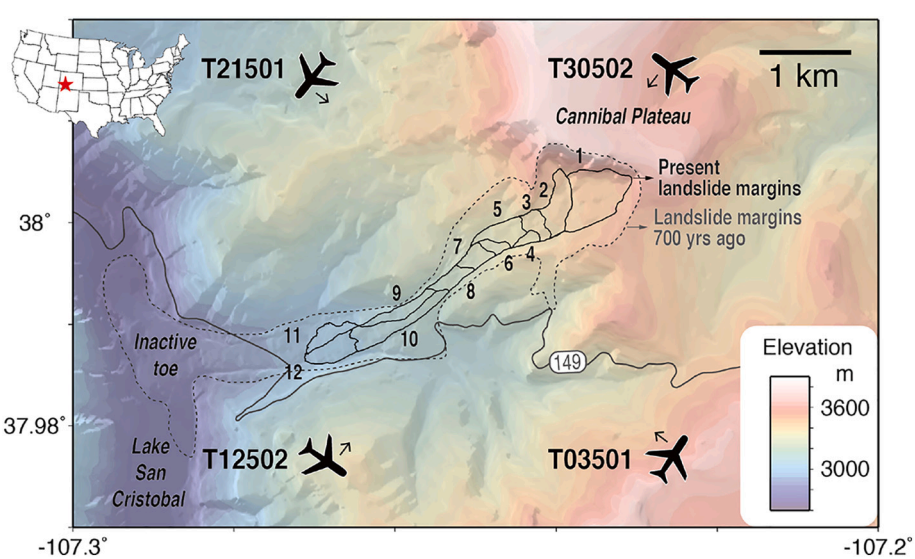

Fig. 1. Topography of the Slumgullion landslide in southwestern Colorado, USA from USGS National Elevation Database. Dashed and solid closed lines show the margins of the prehistoric landslide that formed about 700 years ago and the present active kinematic elements (1–12), modified from (Parise and Guzzi, 1992; Schulz et al., 2017; Hu et al., 2020). The line-of-sight, a.k.a., range directions, of four UAVSAR flight lines are marked by arrows.

structures bound well-defined KEs, i.e., portions of the landslide that move more coherently (Fig. 1). They were first determined by field mapping of morphometric features in 1991, not with geodetic measurements of active deformation (Parise and Guzzi, 1992). The internal deformation of the landslide also alters the landscape such as the development of ponds, and tilted, split and stretched trees (Parise and Guzzi, 1992; Fleming et al., 1999). The landslide materials are composed of hydrothermally altered volcanic rocks and are rich in clay and silt (e.g., smectite and kaolinite). This dynamic hummocky landscape, decorated by various geological features, together with a strong smell of sulfide at the site, make a visit to the Slumgullion landslide a remarkable experience, especially when under the influence of altitude sickness.

2.2. Previous geodetic studies

This prehistoric and reactivated landslide system has been recognized and studied since the 1800s (e.g., Endlich, 1876). The landslide speed was first evaluated by comparing photographs taken at different times (e.g., Crandell and Varnes, 1961; Fleming et al., 1999). During the last few decades, geodetic point-based, e.g., creepmeters, extensometers, theodolite, Global Positioning System (GPS) and area-based, e.g., optical imagery and Synthetic Aperture Radar (SAR) techniques have been employed to measure the landslide deformation.

In terms of the point-based observations, Jackson et al. (1996) used GPS measurements at seven sites during 4 days in June 1993 and estimated displacement rates to be 12–15 mm/day in the center of the active slide. Savage and Fleming (1996) used three extensometers to measure the differential motion across the landslide margin for 9 months starting April 1993 and found an increased sliding rate in the spring. Coe et al. (2000) obtained six sets of nineteen GPS observations during 2-day-long field campaigns between July 1998 and July 1999. The GPS data revealed that the landslide speed peaks between May and July in the middle and upper parts, whereas it peaks between March and May in the lower parts, which might be due to warmer temperatures and earlier snow melt at the ~500-m lower elevation (Coe et al., 2003). Schulz et al. (2009b) used an extensometer to capture the landslide movements from July 2004 to October 2007. The extensometer data, complemented by borehole pore-pressure observations, show that landslide accelerations coincide with water table increases within the landslide body, while the pore pressure near the marginal shear zone drops, suggesting increased shear-induced dilation along the margins during landslide speed-up. Schulz et al. (2009a) compared hourly samples of extensometer-derived landslide speed with atmospheric pressure changes in March 2008 and found that daily accelerations are correlated with diurnal low tides of the atmosphere. Gomberg et al. (2011) relied on conventional robotic theodolite and extensometer measurements together with seismological observations during August 18–26, 2009 and provided qualitative evidence that dilatant strengthening along the margins regulates the landslide motion, as the increased slip velocity is concomitant with an increased frequency of stick-slip events along the lateral surfaces. Coe (2012) analyzed GPS data from twelve summer field campaigns during 1998–2010 to show a correlation between multi-annual changes of landslide motion and a regional moisture-balance index, which is derived from precipitation and temperature records. Considering the anticipated changes in the moisture-balance drought index, Coe (2012) forecasted slowing landslide motions during future warming climates.

SAR data have been widely used at the Slumgullion, but this is challenged by the rapid deformation of the landslide leading to a loss of coherence and limiting the ability to unwrap SAR interferograms. Milillo et al. (2014) made use of 1-day X-band spaceborne COSMO-SkyMed InSAR pairs between 2010 and 2013, and one set of 1-year-interval pixel offsets to capture the motions of the entire landslide. Delbridge et al. (2016) used L-band airborne UAVSAR data and generated the 3D surface displacement fields for three sets of 1-week-interval interferograms from four tracks, collected in April, May and July 2012, respectively; and applied the 3D displacement field to infer the landslide thickness assuming mass conservation. Relying on another airborne SAR system, the Artemis SlimSAR, Cao et al. (2017) obtained similar displacement results using this compact, modular, and multi-frequency radar system. Wang et al. (2018a) used the 2011–2013 UAVSAR data by tracking the pixel offsets on one single track and decomposing the time-series into linear and sinusoidal components. Hu et al. (2020) used a hybrid InSAR and pixel offset tracking method on 2011–2018 UAVSAR data and InSAR time-series analysis of 2017–2018 Sentinel-1 data to demonstrate the spatiotemporally varying displacements and to infer the landslide channel geometry and subsurface flux. By integrating the horizontal UAVSAR velocities and LiDAR-derived landslide thickness in the toe region, Hu and Bürgmann (2020) were able to estimate its viscosity assuming a Bingham plastic rheology. Instead of using SAR data from air and space, Schulz et al. (2017) applied ground-based SAR operating at Ku-band and measured 1 week of ground motions in the summer of 2010, and also validated the measurements using GPS and extensometer data sets.

3. Data and methods

3.1. Remote sensing data

Taking advantage of the airborne platform, the NASA UAVSAR system is superior to the spaceborne missions in its submeter-level resolution (0.6 m in azimuth and 1.67 m in range), which improves our ability to characterize small-scale geological features in landslide terrain. We started with the freely available UAVSAR single-look complex (SLC) stack products that are already precisely coregistered using the GPS unit of the aircraft and the data itself to estimate and compensate for the variable motion between the tracks acquired by the NASA-JPL UAVSAR team (Hensley et al., 2009; Hensley et al., 2010; Bekaert et al., 2019). The DEM used for motion compensation and topographic correction is from the Shuttle Radar Topography Mission (SRTM) 1-arc-second (~30 m) version 2 acquired in 2000. In practice, the airborne UAVSAR system is operated on a modified NASA Gulfstream III airplane and has typical perpendicular baselines $B_\perp$ of ~2 m and platform height h_p of 12,500 m. Using the standard height sensitivity equations for InSAR (e.g., Rosen et al., 2000), we can calculate the displacement error Δd_{los} due to an elevation error Δh_t.

$$\Delta d_{los} = \frac{\lambda}{4\pi}\left[\frac{\partial\phi}{\partial h}\Delta h_t = \frac{4\pi B_\perp \Delta h_t}{\lambda\, p \sin\theta} = \frac{4\pi B_\perp \Delta h_t}{\lambda \frac{h_p}{\cos\theta}\sin\theta}\right] = \frac{B_\perp \Delta h_t}{h_p \tan\theta}$$

where λ is the radar wavelength, p is the slant range distance, and θ is the look angle.

With the largest possible perpendicular baseline $B_\perp$ (say 5 m) and the largest DEM error Δh_t (say 20 m), the line of sight maximal deformation error Δd_{los} is 4.6 mm, which is negligible for Slumgullion moving at dozens of mm per day (S. Hensley, pers. comm. 2020).

$$\Delta d_{los} \le \frac{5 \times 20}{12500 \times \tan 60^\circ} = 4.6\ mm$$

The L-band (wavelength ~ 0.238 m) SAR sensor is also advantageous for maintaining coherence, compared to C- or X-band systems, although the volumetric decorrelation from vegetation is insignificant at Slumgullion. The prehistoric rapid failure and contemporary persistent movement have cleared most vegetation and only a few young trees remain, in contrast to the dense forest cover off the slide. On the other hand, snow cover during the wintertime is an inevitable natural phenomenon that dramatically deteriorates the coherence. Therefore, UAVSAR campaigns at Slumgullion were only deployed between April and November, except for one set of test flights during February and March 2017 not included in the analysis. In addition to the advantage of reduced volumetric decorrelation, the longer wavelength of L-band SAR

Table 1
2011–2018 UAVSAR acquisitions over Slumgullion.

	Reference	Secondary	Days	T30502	T03501	T12502	T21501	Independent observations
1	20110812	20110819	7	+	+	+	+	4
2	20120416	20120423	7	+	+	+	+	4
3	20120423	20120509	16	+	+	+	+	4
4	20120509	20120517	8	+	+		+	3
5	20120724	20120801	8	+	+	+		3
	20130422	20130503	11	+				1
6	20130503	20130510	7	+	+	+	+	4
7	20130510	20130520	10	+	+		+	3
	20131025	20131101	7	+			+	2
8	20140401	20140404	3	+	+	+		3
9	20150428	20150504	6	+	+	+	+	4
10	20150504	20150512	8	+	+	+		3
11	20160616	20160623	7	+		+	+	3
12	20161020	20161027	7	+		+	+	3
13	20171018	20171025	7	+	+	+	+	4
14	20171025	20171101	7	+	+	+	+	4
15	20180725	20180802	8	+	+	+	+	4
16	20181003	20181010	7	+	+	+	+	4

The symbol "+" means that data were acquired on both dates along the indicated flight line. Interferometric pairs are used for 3D displacement inversion when the number of independent observations is greater than three. All the listed interferograms are used for detecting high phase gradients.

also results in less condensed InSAR fringes, which is favorable for unwrapping.

The National Center for Airborne Laser Mapping (NCALM) collected the 0.5-m resolution LiDAR DEM at Slumgullion in July 2015 using an Optech Gemini near-infrared (NIR) LiDAR system (Cao et al., 2017) with an average of 40 pulses per square meter over the main landslide body. Since the Gemini system can measure up to four returns from each laser pulse, both a digital surface model (DSM) and a bare-earth DEM were obtained. In this study, we use the freely available bare-earth LiDAR DEM gridded and archived in OpenTopography to map the morphologic and structural features (Sections 4.4 and 5.1) and to infer the slope aspects (Section 5.2).

3.2. Meteorological data

A snow telemetry (SNOTEL) weather station (#762 at elevation 3523 m), operated by the U.S. Department of Agriculture Natural Resources Conservation Service and National Water and Climate Center, is located ~3200 m southeast of the Slumgullion landslide (elevation 3000–3700 m). Two independent sensors are used to measure the daily precipitation using transducers: the standing precipitation gauge captures and combines all forms of precipitation (rain and snow), and the snow pillow on the ground captures the existing amount of snow (converted to the equivalent thickness of water, a.k.a., snow water equivalent, SWE).

Wind brings substantial uncertainties to the meteorological measurements. For example, the SWE sometimes unexpectedly exceeds the precipitation accumulation. This is because the precipitation gauge can "undercatch" the true amount that fell on windy days. While this can happen with both rain and snow, the issue is more prevalent with snow because it is more easily blown around by the wind. Beyond that, wind may blow additional snow onto the SWE pillow which lies on the ground surface, causing that data to surpass the accumulated precipitation (Karl Wetlaufer, pers. comm. 2019). Hence, we need to use the data collected at a single site with some caution.

Seasonality of precipitation is modest when considering the combined contributions of snow and ice. After integrating the precipitation gauge and SWE data, we find the precipitation mainly falls as snow from October to April and as rain for the rest of the year. The snowpack on the ground starts to melt in April as temperatures rise, with earlier melting at lower elevations and later melting at higher elevations. The fastest melting occurs in May and ends by the end of May or early June. The driest months of the year are June and July. Water year 2018 (October 2017 to October 2018) represents an outstanding drought year (~400 mm annual total), accounting for only 61% of the 1981–2010 average (~640 mm annual total), and 45% of the wettest year 1999 (~880 mm annual total) since the SNOTEL record started in 1980 (ref: https://www.wcc.nrcs.usda.gov) (Fig. S1A).

3.3. SAR interferometry and three-dimensional displacement extraction

The performance of InSAR at Slumgullion is challenged by high displacement gradients that occur over short distances. The maximum resolvable displacement gradient of InSAR occurs when one full fringe fills up a single pixel (Baran et al., 2005). One fringe corresponds to the line-of-sight or range displacement of one half of the radar wavelength. To enhance the coherence, we apply 12 and 3 looks in the azimuth and range directions, respectively, corresponding to a pixel dimension of ~7 m. Multi-looking can enhance the coherence but comes with reduced spatial resolution. We found that interferograms of 12 by 3 looks and 1 by 1 looks are very similar. Using single-look InSAR will not change our observations and the conclusions of this study. The consequent maximum detectable displacement gradient is 1.7×10^{-2} (Hu et al., 2020). Phase aliasing occurs when the time intervals increase to more than about 1 month, and thus phase unwrapping across the rapidly deforming sections of the landslide is no longer possible. We finally use the 16 short-time-interval (3–16 days) UAVSAR InSAR pairs with observations from three or four flight lines for the time-series displacement analysis (Table 1).

Occasionally, long-wavelength ramps are evident for some InSAR-derived displacement fields that may be associated with water vapor gradients and aircraft orientation (yaw and pitch) changes (Jones et al., 2010). The InSAR errors due to inaccurate knowledge of the aircraft motion has a long spatial scale, roughly 5–10 km, much larger than the size of the landslide. Atmospheric delay gradients are common for this landslide with an elevation difference of 700 m from head to toe (Parise and Guzzi, 1992). Given the limited number of acquisitions, the small size of the target area and high displacement gradients, the use of time-series inversion or independent weather models is not feasible to mitigate these atmospheric artifacts. Instead, we estimate a linearly fitted plane from off-slide targets to simulate and remove atmospheric phase and aircraft motion error components.

A unique characteristic of the UAVSAR campaigns at the Slumgullion is that the sensor images the same displacement field spanning the same dates from up to four flight lines and thus different lines of sight. When three or more observations are available for the

given time span, we can invert for the complete 3D displacement field through the least-squares inversion (e.g., Hu et al., 2016; Delbridge et al., 2016),

$$G \bullet m = d$$

where $d_{n\times 1}$ contains the InSAR range-change observations, $G_{n\times 3}$ is the transformation matrix representing the east, north and up look vectors at the target pointing from the aircraft to the ground, which are available for each scene from the UAVSAR website, $m_{3\times 1}$ is the 3D displacements to be solved; and n equals 3 or 4 in this study. We then divide the 3D displacements by the time interval to calculate the velocity and average over the 16 date pairs with at least three independent observations (numbered in Table 1).

3.4. Kinematic elements (KEs) outlined by wrapped interferograms

Lineations of high active displacement gradients on the ground surface mirror the shallow geological discontinuities and associated fault structures. Maps of InSAR-derived velocities and velocity gradients can be used to identify localized deformation along tectonic faults (e.g., Price and Sandwell, 1998; Chaussard et al., 2015; Qu et al., 2015; Hu et al., 2018b). Here we propose a simple method to extract the boundaries of the KEs based on the interferograms before unwrapping (i.e., wrapped interferograms referred to as "interferograms" hereafter). In this case, we can also use interferograms with dense fringes where the correctness of subsequent unwrapping is not guaranteed. Interferograms have abrupt phase changes from -π to π where the unwrapping algorithm is expected to either add or subtract 2π, yet the phase changes are sometimes ambiguous. The purpose of our method is to locate consistently high gradients in wrapped phases after adjusting to different reference points by conjugate multiplication of the complex value of the reference with every pixel in the scene, which is in essence phase subtraction. The use of multiple distributed reference points in each iteration introduces randomness in the positions of phase changes from -π to π; whereas the actual high displacement gradients remain stationary. Applying this procedure at Slumgullion, we first select reference points distributed on- and off- the landslide and consider two cases. In the first case, we use a total of 947 reference points regularly distributed in space ("x" in Fig. 2A). In the second case, we rely on only twelve reference points at specified locations (circles in Fig. 2A): one close to the active toe in the non-deforming downhill area, and the other eleven at the geometric centers of KEs 2–12; we do not consider KE 1 at the upper head because it often lacks coherent targets due to snow cover in late fall and early spring while the majority of the slide has already cleared. For both cases, we adjust the interferograms to those individual references. Second, we calculate the spatial phase gradients in the horizontal north $\left(\frac{\partial d}{\partial x}\right)$ and east $\left(\frac{\partial d}{\partial y}\right)$ directions given by $\sqrt{\left(\frac{\partial d}{\partial x}\right)^2 + \left(\frac{\partial d}{\partial y}\right)^2}$ (e.g., Fig. 2B). Finally, we stack the gradients from the individual reference cases, allowing us to determine the targets always exhibiting high gradient values. This procedure is repeated for each interferogram and each flight line, and the gradient scores are summed and normalized. The merits of this method are severalfold. First, it provides an efficient and automatic routine to identify structural units moving at disparate rates. Second, it avoids unwrapping so that interferograms with complicated phase patterns, for example those with longer time spans, remain usable (Table 1). And third, it is a geo-referenced analysis and thus data from different platforms with variable trajectories and spatial resolutions can be easily integrated. We also apply this phase-gradient routine on C-band spaceborne Sentinel-1 data to outline the structures. Although the results are less clear than those from UAVSAR due to the reduced coherence and coarser resolution, their consistency in the general patterns provides the validation of our approach (Fig. S2).

4. Results

4.1. Distinct phase patterns among the kinematic structures

The UAVSAR interferograms of the Slumgullion landslide represent ideal examples to illustrate the distinct phase representations of the same displacement field from varying slant-looking trajectories (Fig. 3). In examples of 7-day-interval 20110812-20110819 interferograms spanning 1 week, the phase changes and the inferred movements are modest in images obtained from flight lines T21501 and T03501 from perspectives almost normal to the slip direction, such that the movements are in the dead zone of the aircraft. On the other hand, the phase changes are distinct from the perspectives of the other two flight lines. In another example of 16-day-interval 20120423-20120509, the deformation gradients at the boundaries between adjoining KEs 5–7 are not well resolved in flight lines T21501 and T03501, but these slide-parallel looking lines clearly capture the movement and boundaries of KE 11 at the northern tip of the toe.

From the positions of high phase gradients in the interferograms, we remap the margins of the landslide and its KEs and compare our results with the margins mapped in field surveys of associated fault structures

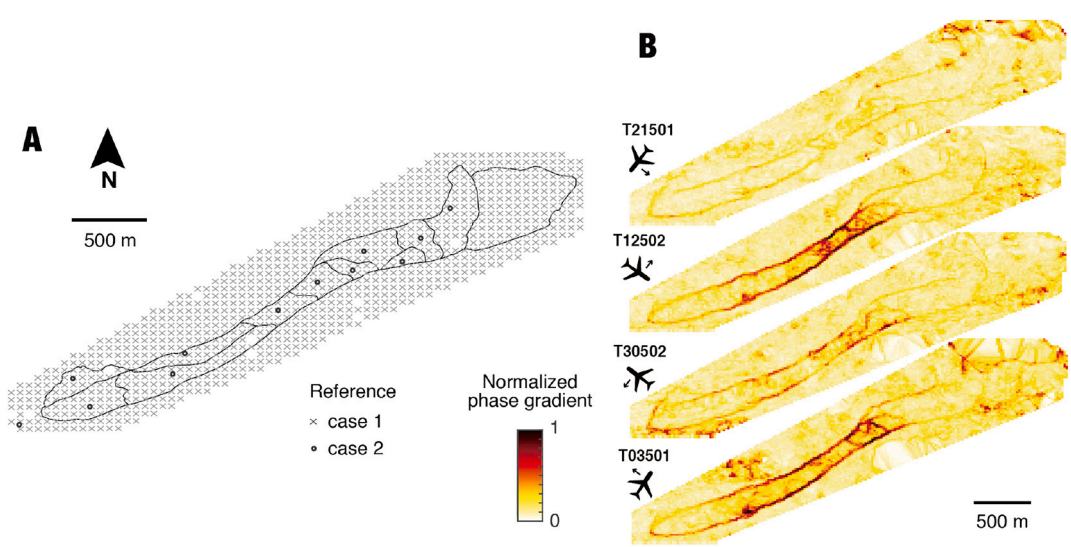

Fig. 2. Determination of landslide margins from multiple reference points. (A) The distribution of reference points: case 1 "x" and case 2 "o". Some blanks are left in generally low coherence areas in case 1. (B) The normalized phase gradients determined from each of the four flight lines in case 2.

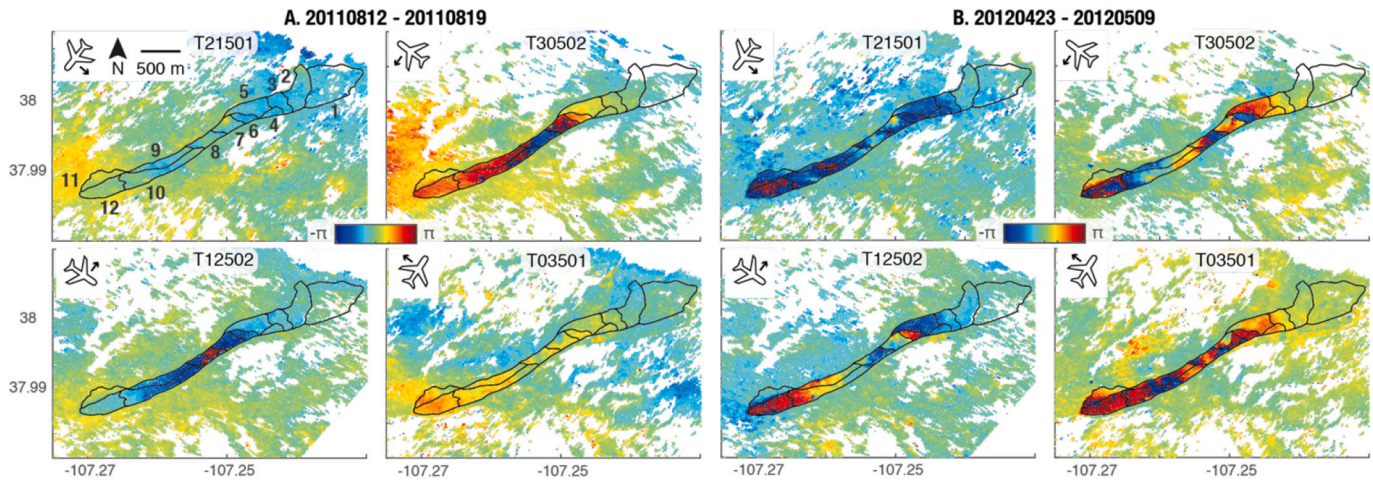

Fig. 3. Examples of wrapped UAVSAR interferograms imaged from different flight lines during two campaigns. (A) 20110812-20110819 (7 days). (B) 20120423-20120509 (16 days). One 2π phase cycle corresponds to 119-mm (half of radar wavelength) change in radar range directions (arrows besides the icons of aircraft).

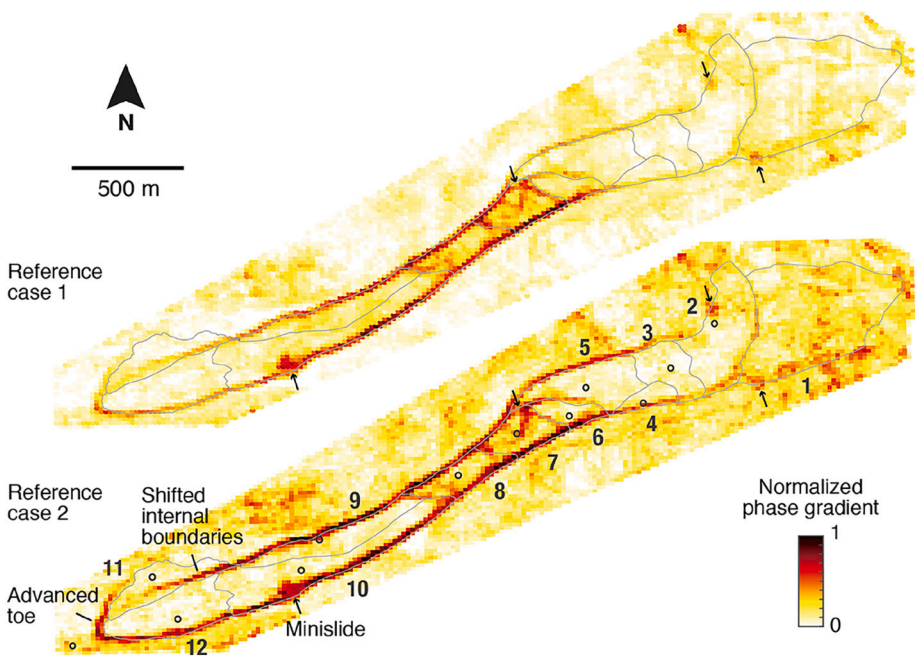

Fig. 4. The landslide structural margins and kinematic elements inferred from the normalized phase gradients for two reference cases. The margins and kinematic elements mapped in 1991 (Parise and Guzzi, 1992) are superimposed as gray lines for comparison. Black circles show the positions of 12 individual reference points used in the phase gradient analysis for case 2 (see Section 3.4). Black arrows indicate apparent minislides.

employed more than two decades earlier (Parise and Guzzi, 1992). Fig. 4 shows the normalized phase gradients for two reference cases, produced by summing and normalizing phase gradients from all interferograms and flight lines with respect to a different set of reference points (Section 3.4). High gradients in red delineate the landslide external margins and boundaries of some of the kinematic elements, including apparent minislides marked with black arrows. It turns out that the margins are better resolved when applying fewer (Cohen-Waeber et al., 2018) but tailored reference points, rather than many (947) but blindly selected reference points. For the multiple, random references case, both the signal and noise are enhanced, and the consequent signal-to-noise ratio declines in this study site. Overall, our simple method can effectively extract the external margins. The edge of the toe apparently shifted by ~40 m downhill from its location mapped in 1991 (Parise and Guzzi, 1992), suggesting an average toe advance rate of ~1.5 m/yr between the UAVSAR data span (2011–2018) and the field survey (in 1991). Internal boundaries of many of the kinematic elements can also be resolved. A sharp phase gradient delineates the interface between KEs 11 and 12, and its position is shifted to the north by ~50 m compared to that in the 1991 map. The fastest and narrowest KEs 6–8 are also separated by bands of high phase gradient, although their distribution is somewhat patchy. This suggests that the longer-term landslide deformation not only advanced the margin at the frontal toe, but also relocated some of the internal KE boundaries. Moreover, we also pick up several apparent secondary minislides near the external margins (red patches pointed by arrows in Fig. 4) (Fleming et al., 1999), e.g., one on the southern edge of KE 1, one on the northern margin of KE 2, one at the conjunction of KEs 5–7 (reddish patches marked with arrows in Fig. 4) and also confirmed a previously identified secondary minislide near the southern margin of KE 10 (Delbridge et al., 2016).

4.2. Three-dimensional displacements

The 3D velocity maps from the average of the 2011–2018 UAVSAR measurements clearly reveal the magnitude and orientation of the landslide movements (Fig. 5). Like most low-gradient translational landslides, the Slumgullion moves primarily horizontally, and the spatial distribution of the inferred vertical motions is less coherent than the horizontal motions. The upper part of the landslide (KEs 1–5) moves consistently at up to 5 mm/day. Landslide speed changes abruptly in

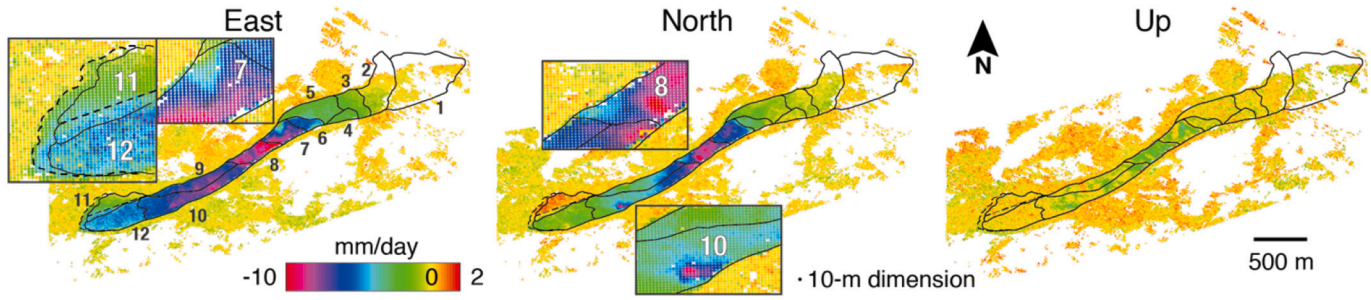

Fig. 5. Three-dimensional surface velocities of the Slumgullion landslide averaged over 2011–2018 observations. Each dot has a 10-m dimension. The solid curves show the landslide external margins and internal boundaries mapped in 1991 (Parise and Guzzi, 1992), and the dashed lines show their shifted location at the toe inferred from the UAVSAR results.

the EW direction at KE 6 where the landslide channel becomes narrow. The adjacent KEs 6 and 7 have a sharp change of displacement in the NS direction. The narrowest KE 8 moves the fastest, with more than 10-mm/day horizontal motion. The northern part of the toe (KE 11) stands out by its northward motion at up to 2 mm/day. The high-resolution displacement maps also reveal some high-frequency signals in the main body of the landslide, likely due to irregular basal surfaces and discontinuous geological structures. Some isolated deforming zones near the lateral margins (e.g., within the northwestern KE 7, southwestern KE 8, the southern side of KE 10) may suggest secondary minislides that we also noted in the previous section, and we will discuss the one in KE 10 in detail.

4.3. Time dependent landslide speed

To investigate the time variations of the landslide speed, we take the spatial average of the 3D velocities over each of the kinematic elements (Fig. 6) and compare it to the estimated water content in the landslide. As the fluid form of water recharge is the key to regulate the pore pressures and thus the landslide motion, we infer the daily fluid water from snowmelt and rainwater using a temperature-based model and data simulation (Hu et al., 2020). The average daily water recharge from rainwater and snowmelt for the time periods considered is up to 16 mm/day (20120423-20120509). Assuming diffusive transport, the normalized modeled pore pressures (Hu et al., 2020) at a nominal 10 m depth seems to only correlate with the first-order variations of the landslide speed, mostly evident in the east direction (Fig. 6A). The time series comparison between landslide velocities and precipitation at the minislide also presents some correlation (Fig. 7C). During the observing period from 2011 to 2018, the landslide moved the fastest in 2015 and the slowest in 2018, corresponding to relatively high and low water years, respectively (Figs. S1A & 6B). However, the linkage of landslide motion to the modeled pore pressure is not well established (R-square is 0.21) as the daily rates are constrained by results from only a few days () and pore pressure comes from a simple 1D model not accounting for local variations in recharge from the inferred snowmelt and rainwater. The poor temporal resolution of the UAVSAR data limits our ability to reveal seasonal variations of the landslide speed, which were documented from daily GPS observations (Coe et al., 2003; Schulz et al., 2009a, 2009b, 2017). The median absolute deviation, i.e., median[abs (X – median(X))], of the daily landslide speed is estimated within each KE as a proxy for decorrelation, and large values are common when snow partially covers the slope in winter and spring, such as in the April 2015 and October 2018 interferograms (Fig. 6C). The relationship between the forms of precipitation and fluid recharge (e.g., from rainwater only, snowmelt only, undistinguishable, or none) and the landslide velocity is not evident (Fig. S1B).

4.4. Spatiotemporal displacements of the secondary minislide

A small, secondary mobile body on top of the Slumgullion landslide, the "minislide" (Delbridge et al., 2016), appears in an isolated area within KE 10. The identification of such nested minislides is not new (e.g., Fleming et al., 1999; Delbridge et al., 2016), but here we investigate its geometry and structural setting, its spatiotemporal behaviors and plausible mechanisms of its formation (more discussion in 4.1). The LiDAR DEM reveals that surface fractures and asperities, such as bumps and depressions, are clustered in this local area. We find several successive curvilinear features at the minislide toe that are indicative of shortening and thickening. In addition, we observe a lazy *Z*-shaped depression, reminiscent of a pull-apart basin (more discussion in 4.1) at the internal head (Fig. 7A). The dimensions of the minislide are about 100 by 70 m. Relative to the main landslide body, it moves southward towards the southern flank of the Slumgullion. The temporal motion of the minislide with respect to a reference point on the adjacent landslide mass (Fig. 7C) is similar to that of the whole landslide as described in Section 4.3. That is, it moved the fastest in wet 2015 and slowed down substantially in dry 2018.

5. Discussion

5.1. Persistency and evolution of kinematic elements

A comparison between the 2011–2018 InSAR-phase-determined external margins and internal boundaries and those from the 1991 field mapping (Parise and Guzzi, 1992) indicates overall consistency (Fig. 4), suggesting a coherent slow movement without substantial changes in the overall extent of the landslide body and arrangement of the principal internal kinematic structures during the last two to three decades. Considering the landslide material moves at a couple of centimeters per day, the material in fastest narrow sections moved by more than 100 m during that period. However, no evident shift of internal kinematic boundaries in the neck region of the Slumgullion is observed. This seems to suggest that these kinematic discontinuities are able to maintain stationary while the landslide materials are transported continuously through them. Similarly, Coe et al. (2009) documented that the location of eight ponds on the Slumgullion remained stationary for ~60 years, suggesting that the pond locations reflect depressions along the underlying basal surface of the landslide. The locations of persistent surface features, such as active internal fault zones and hydrological features, seem to be an imprint of relatively stable basal irregularities (Coe et al., 2009). On the other hand, the internal boundaries within the emergent toe and the frontal tip of the Slumgullion have advanced by several tens of meters during recent decades as the landslide overrides the downslope terrain.

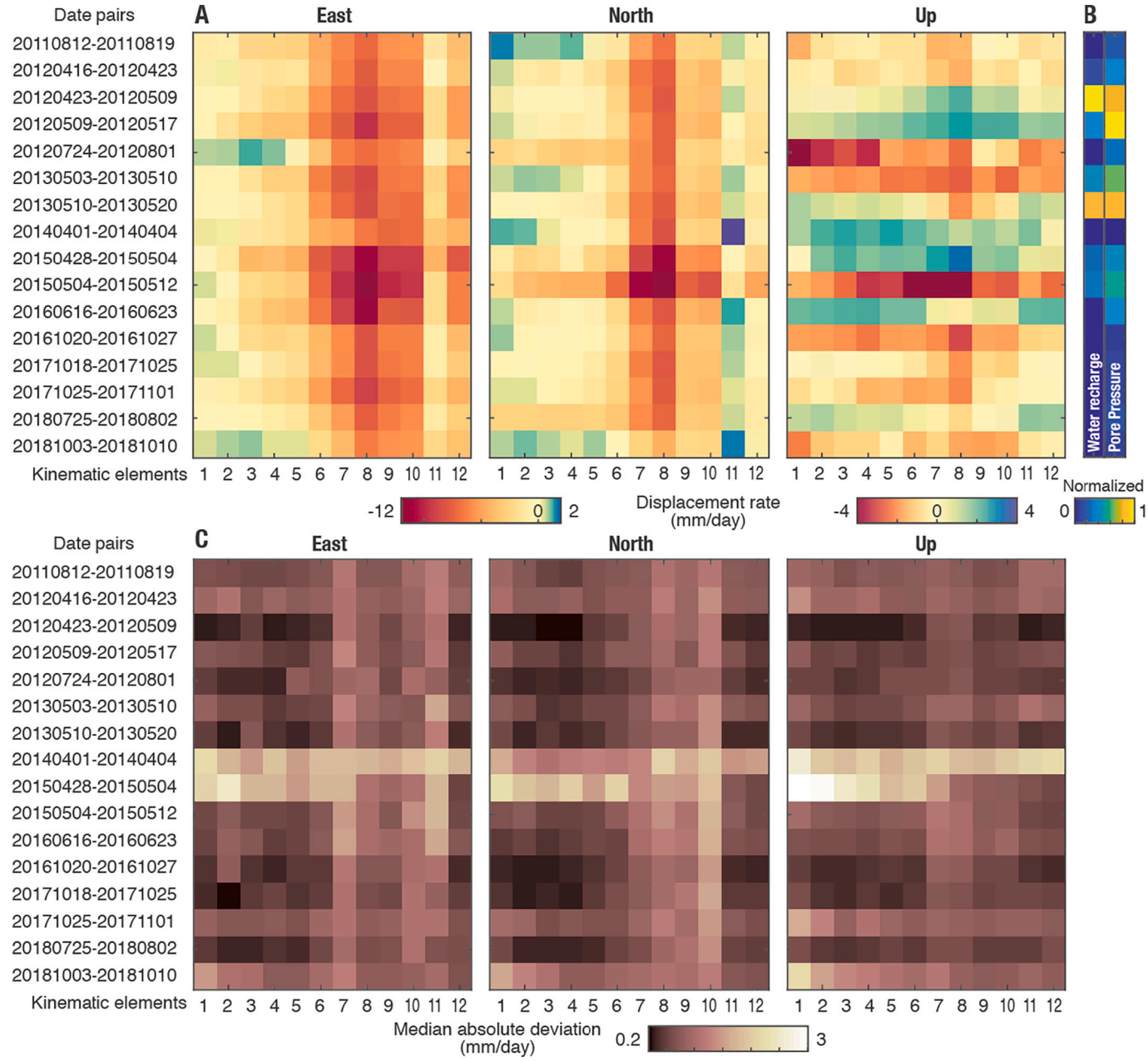

Fig. 6. Variations of landslide speed in space and time. (A) The spatial average 3D velocity components (mm/day) and (C) median absolute deviation of daily landslide speed of the twelve kinematic elements for the time spans indicated. KE 11 presents northward motion with positive values (dark blue); otherwise, most of the active areas move westward and southward. (B) The normalized results of the average daily water recharge and the modeled pore pressure at nominal 10 m depth for each time period considered (Hu et al., 2020). (For interpretation of the references to colour in this figure legend, the reader is referred to the web version of this article.)

5.2. Horizontal vector comparison between UAVSAR InSAR results and LiDAR DEM

Spaceborne InSAR is sensitive to vertical and EW motions due to its polar orbits along ascending or descending trajectories. The consequent look vectors from all existing satellite SAR missions are nearly identical from the same orbital direction, i.e., ascending or descending. This will change in the future when the NASA-ISRO SAR (NISAR) mission is launched (planned for 2022) as it will operate with a left-looking or slightly south-looking SAR that is different from other SAR satellites that look to the right or slightly north. There are other analysis methods for satellite SAR that can measure along-track motion at coarser resolution, including pixel offset tracking and multiple-aperture or along-track interferometry. These are less accurate than standard InSAR, so 3D displacements using those measurements have less sensitivity to the north component of motion. To resolve a quasi-3D displacement field with existing satellites at full resolution, it is usually assumed that there is no NS motion, or some constraints are added on the moving directions, such as fault-parallel in context of strike-slip faulting or downhill motion for mobile slopes. Thanks to the versatile airborne UAVSAR flight lines, we are able to extract the complete 3D displacements at full resolution and are thus able to test the latter assumption. Here we investigate the consistency of the horizontal slip directions measured by UAVSAR interferograms and the downhill aspects estimated from the 0.5-m resolution LiDAR DEM (Lee, 2015) (Fig. 8). Since this landslide surface has been highly modified, the 0.5-m resolution LiDAR DEM reveals great morphological complexity, but it can't yield a sensible slope aspect unless being downsampled. Assuming the slope of the basal

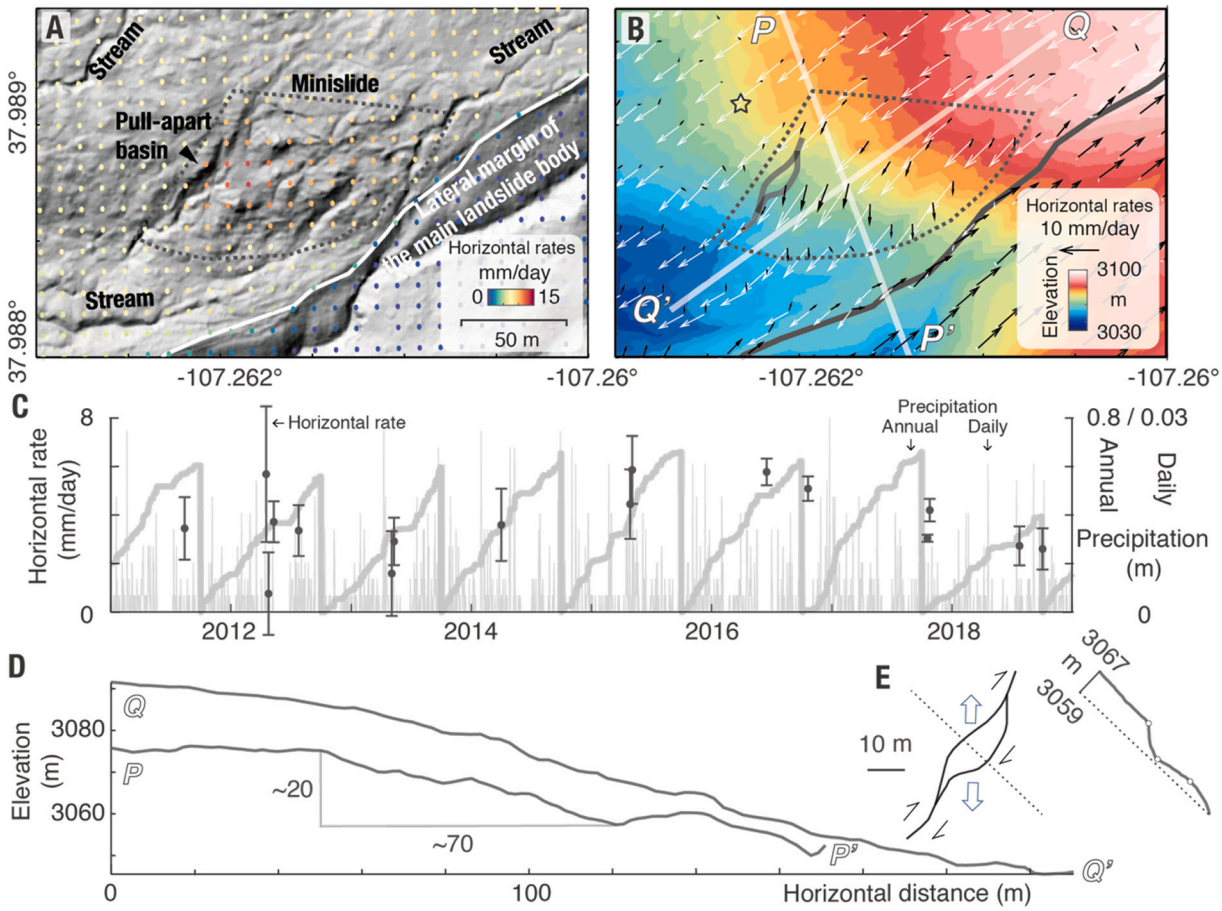

Fig. 7. Kinematics and surface structures at the secondary minislide. (A) The morphology of the minislide in shaded relief of LiDAR DEM superimposed by the horizontal displacement rates. The SW trending white line represents the lateral margin of the main landslide body. (B) Surface elevation superimposed by the horizontal velocity vectors. The black arrows are relative to an on-slide reference point to the NW of the minislide indicated by the black star; white arrows are with respect to the off-slide inactive terrain. Gray dotted lines outline the fan-shaped minislide. (C) The correlation between horizontal rates measured by UAVSAR InSAR with reference to the on-slide reference point and the daily and cumulative annual precipitation, reset to zero on October 1st. The error bars represent the mean absolute deviation of targets within the minislide. (D) Elevation profiles PP' and QQ' along the white line shown in panel B. (E) A conceptual sketch of right-lateral strike-slip faulting creating a pull-apart basin. A cross-sectional elevation profile reveals a local depression of 3.85 m.

surface follows the long-wavelength morphology of the ground surface, it is important to apply the downsampling. Here we resample the DEM by averaging boxes of 100 m and 300 m across to preserve the main topographic features before calculating the slope. Large variability in the DEM-derived slope aspects from different resampled spacing is evident in the steep head, the spreading-out toe, and the bends. There is no consistent answer on which of the downsampled DEM aspects fit the UAVSAR-derived vectors better. UAVSAR results are more consistent with the aspects generated by the 300-m DEM for the steep KEs 6 and 7, but for KE 10, the use of the 100-m DEM results in more consistency. Nonetheless, UAVSAR-measured landslide motion directions are unlike the slope aspects of either of the downsampled DEMs near the margins due to the edge effect of downsampling and slope aspect computation, for example, around the southern flanks of KE 12. Therefore, relying on a DEM to estimate the downhill movement from slant-looking SAR observations (e.g., Hilley et al., 2004; Hu et al., 2016) may be

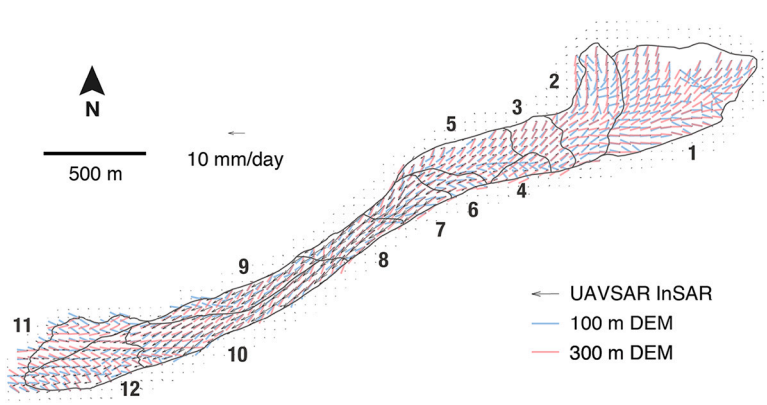

Fig. 8. Horizontal displacement vectors inferred from UAVSAR InSAR and 0.5-m resolution bare-earth LiDAR DEM, downsampled to 100 m and 300 m, respectively.

problematic in some places due to the heterogeneous nature of landslide deformation processes.

5.3. Hypothesis on the formation of the secondary minislide

The internally deforming and crumbly nature of the debris slide constantly creates and destroys geological features at the Slumgullion (Fleming et al., 1999). The persistence of the secondary minislide is enigmatic and remarkable and leads us to explore its initiation and kinematics. The minislide is nested in an oversteepened area along the Slumgullion main body. The elevation profiles PP' and QQ' indicate ~20-m topographic relief within a horizontal distance of ~70 m, constituting a local slope of ~16° (Fig. 7B& D), twice of the average slope for the entire landslide (Parise and Guzzi, 1992). Importantly, multiple sub-parallel strike-slip faults near the landslide margins gave birth to the secondary pull-apart basins which help enlarge the lateral channel width towards the distal end of the landslide. In particular, the sides of the minislide overlap with geomorphological features of a pull-apart basin. The dimensions of this depressed basin are about 30 by 10 m (Fig. 7E), and the consequent length-to-width ratio of three agrees well with observations of the geometry of pull aparts in natural tectonic regimes worldwide ranging from tens of meters to tens of kilometers in length (e.g., Aydin and Nur, 1982), and also falls in the range of 2.2–3.8 found in experimental models (e.g., Basile and Brun, 1999). The acute angle between the oblique bounding faults of this pull-apart basin is almost 30°, consistent with a typical range of 30°-35° (e.g., Gürbüz, 2010). The depth of the pull-apart basin is predicted to be 2.44 m according to an empirical relationship with the length and width given by $d = 0.1104 \cdot l - (8.755 \times 10^{-2}) \cdot w$ (Gürbüz, 2010), though the actual geometry clearly depends on the complex structures and details of sedimentation rates around the pull apart. On the other hand, the DEM-derived depth is 3.85 m taken from the mean height difference between the bottom to two nearby points at the sides of the inclined slope (Fig. 7E). The measured displacement fields validate the axial right-lateral strike-slip fault zone — the southeastern part moves N223°W at 13 mm/day while the northwestern part moves N124°W at 8 mm/day. Two sub-parallel right-lateral faults with a relative slip rate of ~5 mm/day created the pull-apart basin at their stepover. Overall, the internal toe of the minislide is bounded by streams incised in the landslide deposits. The abrupt increase in the slope angle, localized extension across the upper margin, and the persistent erosion at the internal toe help establish the kinematic environment for the formation of this secondary minislide, and also allow it to be moving more southerly than the surrounding mobile areas.

6. Conclusions and implications

Slow-moving landslides continuously create and destroy geological features during the mass wasting processes. Many of these geological structures formed in the landslide environment are miniatures of those resulting from plate tectonics. In this study, we focus on the Slumgullion landslide in Colorado, a dynamic system that includes various kinematic features. High resolution 3D surface displacement maps from multiple UAVSAR flight lines shed new light on details of the active landslide margins and internal kinematic boundaries. To optimally exploit the UAVSAR interferograms, we propose a simple method to identify distinct kinematic elements from high phase gradients in wrapped interferograms with multiple, distributed reference points. Validated by pre-defined structural maps from field observations and results from different SAR data sets, our method demonstrates confident detection of the external margins and some internal boundaries. We also confirm a shift of the toe edge and an internal boundary by a few tens of meters due to progressive spreading during the past two to three decades previously reported in Hu et al. (2020). This automated and efficient method can also be applied to identify other geological displacement discontinuities such as those found in active fault zones. For a specific secondary minislide developed within the active main body, we analyze its displacements and kinematic characteristics. The shearing of subparallel right-lateral strike-slip faults create a pull-apart basin in between, bounding the upper part of the minislide. The dimensions of this pull-apart basin have similar scalings as those found in tectonic environments. The formation of this minislide can be attributed to local extension from the pull-apart basin along its lateral margin, erosion of its toe by incised streams, and the oversteepened slope at the site. Our results also demonstrate that the actual moving directions within the landslide can substantially deviate from the local slope aspects. Therefore, inferring the downhill movements simply from available DEM data (e.g., Hilley et al., 2004; Hu et al., 2016) needs to be undertaken with caution. In addition, landslide speed variations during the available 16 UAVSAR short observation periods are generally correlated with the water recharge from precipitation and modeled pore-pressure changes from infiltration. Taking advantage of the high-resolution UAVSAR InSAR data, our work illustrates the suitability of airborne geodetic missions for detailed characterization of the internal landslide kinematics and thus for other rapid geological and geomorphological deformation processes.

Declaration of competing interest

The authors declare that they have no known competing financial interests or personal relationships that could have appeared to influence the work reported in this paper.

Acknowledgement

This research was supported by the NASA Earth Surface and Interior Geodetic Imaging program. Part of this research was performed at the Jet Propulsion Laboratory, California Institute of Technology under contract with the National Aeronautics and Space Administration. We thank the UAVSAR flight and data processing teams for providing the SLC stacks (available from https://uavsar.jpl.nasa.gov). We thank Scott Hensley and Karl Wetlaufer for helpful discussions on the UAVSAR InSAR products and precipitation survey products, respectively. The shaded relief map in Fig. 1 is produced from USGS National Elevation Database. LiDAR data acquisition and processing were completed by the National Center for Airborne Laser Mapping (NCALM) funded by NSF's Division of Earth Sciences, Instrumentation and Facilities Program. SNOTEL weather data can be downloaded from the U.S. National Water and Climate Center (https://www.wcc.nrcs.usda.gov/index.html).

CRediT author statement

X.H. and R.B. designed the study. X.H. analyzed SAR images and performed the modeling. E.J.F. planned and coordinated UAVSAR data collection and analysis. H.L. planned and coordinated the LiDAR data collection. X.H. drafted the paper with input from all co-authors.

Appendix A. Supplementary data

Supplementary data to this article can be found online at https://doi.org/10.1016/j.rse.2020.112057.

References

Aydin, A., Nur, A., 1982. Evolution of pull-apart basins and their scale independence. Tectonics 1, 91–105. https://doi.org/10.1029/TC001i001p00091.

Baran, I., Stewart, M., Claessens, S., 2005. A new functional model for determining minimum and maximum detectable deformation gradient resolved by satellite radar interferometry. IEEE Trans. Geosci. Remote Sens. 43, 675–682. https://doi.org/10.1109/TGRS.2004.843187.

Basile, C., Brun, J.P., 1999. Transtensional faulting patterns ranging from pull-apart basins to transform continental margins: an experimental investigation. J. Struct. Geol. 21, 23–37. https://doi.org/10.1016/S0191-8141(98)00094-7.

Bekaert, D.P.S., Jones, C.E., An, K., Huang, M.-H., 2019. Exploiting UAVSAR for a comprehensive analysis of subsidence in the Sacramento Delta. Remote Sens. Environ. 220, 124–134.

Bürgmann, R., Rosen, P.A., Fielding, E.J., 2000. Synthetic aperture radar interferometry to measure Earth's surface topography and its deformation. Annu. Rev. Earth Planet. Sci. 28, 169–209. https://doi.org/10.1146/annurev.earth.28.1.169.

Cao, N., Lee, H., Zaugg, E., Shrestha, R., Carter, W., Glennie, C., Wang, G., Lu, Z., Fernandez-Diaz, J.C., 2017. Airborne DInSAR results using time-domain back-projection algorithm: a case study over the Slumgullion landslide in Colorado with validation using spaceborne SAR, airborne LiDAR, and ground-based observations. IEEE J. Sel. Top. Appl. Earth. Obs. Remote Sens. 10 (11), 4987–5000. https://doi.org/10.1109/JSTARS.2017.2737362.

Chaussard, E., Bürgmann, R., Fattahi, H., Nadeau, R.M., Taira, T., Johnson, C.W., Johanson, I., 2015. Potential for larger earthquakes in the East San Francisco Bay Area due to the direct connection between the Hayward and Calaveras Faults. Geophys. Res. Lett. 42, 2734–2741. https://doi.org/10.1002/2015GL063575.

Coe, J.A., 2012. Regional moisture balance control of landslide motion: implications for landslide forecasting in a changing climate. Geology 40 (4), 323–326. https://doi.org/10.1130/G32897.1.

Coe, J.A., Godt, J.W., Ellis, W.L., Savage, W.Z., Savage, J.E., Powers, P.S., Varnes, D.J., Tachker, P., 2000. Preliminary interpretation of seasonal movement of the Slumgullion landslide as determined from GPS observations. In: U.S. Geological Survey Open-File Report 00-102.

Coe, J.A., Ellis, W.L., Godt, J.W., Savage, W.Z., Savage, J.E., Michael, J.A., Kibler, J.D., Powers, P.S., Lidke, D.J., Debray, S., 2003. Seasonal movement of the Slumgullion landslide determined from Global Positioning System surveys and field instrumentation, July 1998–March 2002. Eng. Geol. 68 (1–2), 67–101. https://doi.org/10.1016/S0013-7952(02)00199-0.

Coe, J.A., Mckenna, J.P., Godt, J.W., Baum, R.L., 2009. Basal-topographic control of stationary ponds on a continuously moving landslide. Earth Surf. Process. Landf. 34 (2), 264–279. https://doi.org/10.1002/esp.1721.

Cohen-Waeber, J., Bürgmann, R., Chaussard, E., Giannico, C., Ferretti, A., 2018. Spatiotemporal patterns of precipitation-modulated landslide deformation from independent component analysis of InSAR time series. Geophys. Res. Lett. 45. https://doi.org/10.1002/2017GL075950.

Crandell, D.R., Varnes, D.J., 1961. Movement of the Slumgullion earthflow near Lake City, Colorado. In: Short Papers in the Geologic and Hydrologic Sciences. U.S. Geological Survey Professional Paper 424-Bpp. B136–B139.

Delbridge, B.G., Bürgmann, R., Fielding, E.J., Hensley, S., Schulz, W.H., 2016. 3D surface deformation derived from airborne interferometric UAVSAR: application to the Slumgullion landslide. J. Geophys. Res. Solid Earth 121, 3951–3977. https://doi.org/10.1002/2015JB012559.

Dong, J., Zhang, L., Tang, M., Liao, M., Xu, Q., Gong, J., Ao, M., 2018. Mapping landslide surface displacements with time series SAR interferometry by combining persistent and distributed scatterers: a case study of Jiaju landslide in Danba, China. Remote Sens. Environ. 205, 180–198. https://doi.org/10.1016/j.rse.2017.11.022.

Endlich, F.M., 1876. Report of F.M. Endlich. U.S. Geological and Geographical Survey of the Territories. Annual Report 1874, P. 203.

Fleming, R.W., Baum, R.L., Savage, W.Z., 1996. The Slumgullion landslide, Hinsdale County, Colorado. In: Colorado Geological Survey Special Publication 44: Geological Society of America Guidebook for Field Trips, 108th Annual Meeting, Denver, Colo., 1996, 23 p.

Fleming, R.W., Baum, R.L., Giardino, M., 1999. Map and description of the active part of the Slumgullion landslide, Hinsdale County, Colorado. In: U.S. Geological Survey Geologic Investigations Series Map I-2672.

Gomberg, J., Bodin, P., Savage, W., Jackson, M., 1995. The Slumgullion earthflow, Colorado: a useful analog to crustal tectonics. Geology 23, 41–44.

Gomberg, J., Schulz, W., Bodin, P., Kean, J., 2011. Seismic and geodetic signatures of fault slip at the Slumgullion Landslide natural laboratory. J. Geophys. Res. 116, B09404. https://doi.org/10.1029/2011JB008304.

Gürbüz, A., 2010. Geometric characteristics of pull-apart basins. Lithosphere 2, 199–206. https://doi.org/10.1130/L36.1.

Handwerger, A.L., Rempel, A.W., Skarbek, R.M., Roering, J.J., Hilley, G.E., 2016. Rate-weakening friction characterizes both slow sliding and catastrophic failure of landslides. Proc. Natl. Acad. Sci. U. S. A. 113 (37), 10,281–10,286. https://doi.org/10.1073/pnas.1607009113.

Handwerger, A.L., Fielding, E.J., Huang, M.H., Bennett, G.L., Liang, C., Schulz, W.H., 2019a. Widespread initiation, reactivation, and acceleration of landslides in the northern California Coast Ranges due to extreme rainfall. J. Geophys. Res. Earth Surf. 124, 1782–1797. https://doi.org/10.1029/2019JF005035.

Handwerger, A.L., Huang, M., Fielding, E.J., Booth, A.M., Bürgmann, R., 2019b. A shift from drought to extreme rainfall drives a stable landslide to catastrophic failure. Sci. Rep. 9, 1569. https://doi.org/10.1038/s41598-018-38300-0.

Hensley, S., Zebker, H., Jones, C., Michel, T., Muellerschoen, R., Chapman, B., 2009. First deformation results using the NASA/JPL UAVSAR instrument. In: 2009 2nd Asian-Pacific Conference on Synthetic Aperture Radar. Xi'an, Shanxi, China, pp. 1051–1055.

Hensley, S., Zebker, H., Jones, C., Michel, T., Muellerschoen, R., Chapman, B., 2010. Use of airborne SAR interferometry for monitoring deformation of large-scale man-made features. In: International Workshop Spatial Information Technologies, Hong Kong.

Hilley, G.E., Bürgmann, R., Ferretti, A., Novali, F., Rocca, F., 2004. Dynamics of slow-moving landslides from permanent scatterer analysis. Science 304, 1952–1954.

Hu, X., Bürgmann, R., 2020. Rheology of a debris slide from the joint analysis of UAVSAR and LiDAR data. Geophys. Res. Lett. 47 e2020GL087452.

Hu, X., Wang, T., Pierson, T.C., Lu, Z., Kim, J.W., Cecere, T.H., 2016. Detecting seasonal landslide movement within the Cascade landslide complex (Washington) using time-series SAR imagery. Remote Sens. Environ. 187, 49–61. https://doi.org/10.1016/j.rse.2016.10.006.

Hu, X., Oommen, T., Lu, Z., Wang, T., Kim, J.W., 2017. Consolidation settlement of Salt Lake County tailings impoundment revealed by time-series InSAR observations from multiple radar satellites. Remote Sens. Environ. 202, 199–209. https://doi.org/10.1016/j.rse.2017.05.023.

Hu, X., Lu, Z., Pierson, T.C., Kramer, R., George, D.L., 2018a. Combining InSAR and GPS to determine transient movement and thickness of a seasonally active low-gradient translational landslide. Geophys. Res. Lett. 45, 1453–1462. https://doi.org/10.1002/2017GL076623.

Hu, X., Lu, Z., Wang, T., 2018b. Characterization of hydrogeological properties in Salt Lake Valley, Utah using InSAR. J. Geophys. Res. Earth Surf. 123. https://doi.org/10.1029/2017JF004497.

Hu, X., Bürgmann, R., Lu, Z., Handwerger, A.L., Wang, T., Miao, R., 2019. Mobility, thickness, and hydraulic diffusivity of the slow-moving Monroe landslide in California revealed by L-band satellite radar interferometry. J. Geophys. Res. Solid Earth 124. https://doi.org/10.1029/2019JB017560.

Hu, X., Bürgmann, R., Schulz, W., Fielding, E., 2020. Four-dimensional surface motions of the Slumgullion landslide and quantification of hydrometeorological forcing. Nat. Commun. 11, 2792. https://doi.org/10.1038/s41467-020-16617-7.

Iverson, R.M., Reid, M.E., Iverson, N.R., LaHusen, R.G., Logan, M., Mann, J.E., Brien, D.L., 2000. Acute sensitivity of landslide rates to initial soil porosity. Science 290 (5491), 513–516. https://doi.org/10.1126/science.290.5491.513.

Jackson, M.E., Bodin, P.W., Savage, W.Z., Nel, E.M., 1996. Measurement of local horizontal velocities on the Slumgullion landslide using the Global Positioning System. In: Varnes, D.J., Savage, W.Z. (Eds.), The Slumgullion Earth Flow: A Large-Scale Natural Laboratory. U.S. Geological Survey Bull. 2130pp. 93–95.

Jones, C., Hensley, S., Michel, T., Muellershoen, R., 2010. Advanced motion compensation for airborne platforms: application to UAVSAR. In: International Geoscience and Remote Sensing Symposium (IGARSS) 2010, Honolulu, HI.

Kang, Y., Lu, Z., Zhao, C., Zhang, Q., Kim, J.-W., Niu, Y., 2019. Diagnosis of Xinmo (China) landslide based on Interferometric synthetic aperture radar observation and modeling. Remote Sens. 11, 1846. https://doi.org/10.3390/rs11161846.

Kim, J.W., Lu, Z., Qu, F., Hu, X., 2015. Pre-2014 mudslides at Oso revealed by InSAR and multi-source DEM analysis. Geomat. Nat. Haz. Risk 6 (3), 184–194. https://doi.org/10.1080/19475705.2015.1016556.

Krzeminska, D., Bogaard, T., Malet, J.-P., Van Beek, L., 2013. A model of hydrological and mechanical feedbacks of preferential fissure flow in a slow-moving landslide. Hydrol. Earth Syst. Sci. 17. https://doi.org/10.5194/hess-17-947-2013.

Lacroix, P., Berthier, E., Maquerhua, E.T., 2015. Earthquake-driven acceleration of slow-moving landslides in the Colca 351 valley, Peru, detected from Pléiades images. Remote Sens. Environ. 165, 148–158. https://doi.org/10.1016/j.rse.2015.05.010.

Lacroix, P., Handwerger, A.L., Bièvre, G., 2020. Life and death of slow-moving landslides. Nat. Rev. Earth Environ. https://doi.org/10.1038/s43017-020-0072-8.

Lee, H., 2015. Slumgullion Landslide, Colorado airborne lidar survey. In: National Center for Airborne Laser Mapping (NCALM), Distributed by OpenTopography, https://doi.org/10.5069/G91834KD.

Lu, Z., Dzurisin, D., 2014. InSAR Imaging of Aleutian Volcanoes: Monitoring a Volcanic Arc from Space. Springer Praxis Books, Geophysical Sciences, ISBN 978-3-642-00347-9. Springerhttps://doi.org/10.1007/978-3-642-00348-6. 390 pp.

Milillo, P., Fielding, E.J., Shulz, W.H., Delbridge, B.G., Burgmann, R., 2014. COSMO-SkyMed spotlight interferometry over rural areas: the Slumgullion landslide in Colorado, USA. IEEE J. Sel. Topics Appl. Earth Observ. Remote Sens. 7 (7), 2919–2926. https://doi.org/10.1109/JSTARS.2014.2345664.

Parise, M., Guzzi, R., 1992. Volume and shape of the active and inactive parts of the Slumgullion landslide, Hinsdale County, Colorado. In: U.S. Geological Survey Open-File Report, 92-216, 29 p.

Price, E.J., Sandwell, D.T., 1998. Small-scale deformations associated with the 1992 Landers, California, earthquake mapped by synthetic aperture radar interferometry phase gradients. J. Geophys. Res. Solid Earth 103https://doi.org/10.1029/98JB01821. B11, 27,001-27,016.

Qu, F., Lu, Z., Zhang, Q., Bawden, G.W., Kim, J.W., Zhao, C., Qu, W., 2015. Mapping ground deformation over Houston–Galveston, Texas using multi-temporal InSAR. Remote Sens. Environ. 169 (2015), 290–306. https://doi.org/10.1016/j.rse.2015.08.027.

Rosen, P.A., Hensley, S., Joughin, I.R., Li, F.K., Madsen, S.N., Rodriguez, E., Goldstein, R.M., 2000. Synthetic aperture radar interferometry. Proc. IEEE 88 (3), 333–382.

Savage, W.Z., Fleming, R.W., 1996. Slumgullion landslide fault creep studies. In: Varnes, D.J., Savage, W.Z. (Eds.), The Slumgullion Earth Flow: A Large-Scale Natural Laboratory. U.S. Geological Survey Bull. 2130pp. 73–76.

Schulz, W.H., Kean, J.W., Wang, G., 2009a. Landslide movement in Southwest Colorado triggered by atmospheric tides. Nat. Geosci. 2 (12), 863–866. https://doi.org/10.1038/ngeo659.

Schulz, W.H., Mckenna, J.P., Kibler, J.D., Biavati, G., 2009b. Relations between hydrology and velocity of a continuously moving landslide—evidence of pore-pressure feedback regulating landslide motion? Landslides 6 (3), 181–190. https://doi.org/10.1007/s10346-009-0157-4.

Schulz, W.H., Coe, J.A., Ricci, P.P., Smoczyk, G.M., Shurtleff, B.L., Panosky, J., 2017. Landslide kinematics and their potential controls from hourly to decadal timescales: insights from integrating ground-based InSAR measurements with structural maps and long-term monitoring data. Geomorphology 285, 121–136. https://doi.org/10.1016/j.geomorph.2017.02.011.

Shi, X., Xu, Q., Zhang, L., Zhao, K., Dong, J., Jiang, H., Liao, M., 2019. Surface displacements of the Heifangtai terrace in Northwest China measured by X and C-band InSAR observations. Eng. Geol. 259, 105181. https://doi.org/10.1016/j.enggeo.2019.105181.

Wang, C., Cai, J., Li, Z., Mao, X., Feng, G., Wang, Q., 2018a. Kinematic parameter inversion of the Slumgullion landslide using the time series offset tracking method with UAVSAR data. J. Geophys. Res. Solid Earth 123, 8110–8124. https://doi.org/10.1029/2018JB015701.

Wang, T., DeGrandpre, K., Lu, Z., Freymueller, J.T., 2018b. Complex surface deformation of Akutan volcano, Alaska revealed from InSAR time series. Int. J. Appl. Earth Obs. Geoinf. 64, 171–180. https://doi.org/10.1016/j.jag.2017.09.001.

Wang, T., Shi, Q., Nikkhoo, M., Wei, S., Barbot, S., Dreger, D., Bürgmann, R., Motagh, M., Chen, Q.F., 2018c. The rise, collapse, and compaction of Mt. Mantap from the 3 September 2017 North Korean nuclear test. Science. https://doi.org/10.1126/science.aar7230. eaar7230.